Journal of African Earth Sciences 58 (2010) 475–488

Contents lists available at ScienceDirect

Journal of African Earth Sciences

journal homepage: www.elsevier.com/locate/jafrearsci

Calc-silicates from Wadi Solaf region, Sinai, Egypt

T.S. Abu-Alam *, K. Stüwe, C. Hauzenberger

Institut für Erdwissenschaften, Universität Graz, Universitätsplatz 2, A-8010 Graz, Austria

ARTICLE INFO

Article history:
Received 10 August 2009
Received in revised form 1 April 2010
Accepted 10 May 2010
Available online 26 May 2010

Keywords:
Pan-African Orogeny
Calc-silicate
T-XCO_2 path
Fluid evolution
Thermodynamic modelling

ABSTRACT

Calc-silicates have proved to be important rock types to place constraints on the fluid behaviour in high grade metamorphic rocks. Here we describe amphibolite facies calc-silicate rocks of Wadi Solaf, Egypt which is one of the highest grade basement complexes of Egypt and was exhumed in close connection with the Najd fault system – one of the largest pre-Mesozoic fault systems on the Earth. Calc-silicates formed around 7–8 kbar in temperature range of 600–720 °C and can be classified into three groups (CS_1, CS_2 and CS_3). CS_1 and CS_2 are characterized by the presence of garnet porphyroblasts which contain concentrically arranged wollastonite inclusions. CS_3 has a similar paragenesis but is characterized by the presence of clinozoisite/epidote and the absence of wollastonite as well as a pervasive late overgrowth of prehnite. Garnet in CS_1 lies along a grossular–andradite solid solution, while the garnet composition of CS_2 and CS_3 is hydrogrossular and hydroandradite. There is a positive correlation between Al_2O_3 and Na_2O as well as between Al_2O_3 and Fe_2O_3 from CS_2 through CS_1 to CS_3 possibly indicating a successive increase in fluid flow between the different calc-silicate types. During the peak metamorphism, the XCO_2 is 0.02–0.08 and 0.2–0.44 for the CS_1 and CS_3, respectively. The mineral assemblage of CS_1 and CS_2 buffered the composition of the fluids along the reaction: q + cc = wo + CO_2. During post-peak metamorphism the rocks were intruded by syn-tectonic granites. CS_2 records the contact metamorphic conditions. The rocks reached a peak contact metamorphism conditions at temperature 790–828 °C and XCO_2 = 0.22–0.41. Finally, the rocks reached a temperature range 296–311 °C during the cooling path.

1. Introduction

Fluid flow in ductile shear zones may have important consequences for the thermal and chemical structure of the crust (e.g. Bickle and McKenzie, 1987; Brady, 1988; Cartwright and Buick, 1995). In order to study this, calc-silicates have proved useful rock types because their parageneses bear information on the ratio of CO_2 and H_2O in the infiltrating fluids and often dependent on the total fluid volume that has infiltrated a given unit (Greenwood, 1967, 1975; Harley and Buick, 1992; Harley et al., 1994; Shaw and Arima, 1996; Hartmann et al., 2008). Many of these studies suggest that fluids are very effective transport media for elements and heat and that the fluid flow can occur as highly channelized flow along more permeable lithologies or structural weaknesses such as shear zones.

The Arabian–Nubian Shield (northern part of the East African Orogen) is cut by a complex system of ductile shear zones known as Najd faults system (NFS) (Moore, 1979) that may be a candidate for such fluid flow. This system is one of the largest pre-Mesozoic zone of transcurrent faulting on the Earth (Stern, 1985) and was developed during the Pan-African Orogeny. It played an important role for the exhumation of high grade metamorphic rocks of the region (Fritz et al., 1996, 2002; Loizenbauer et al., 2001; Abd El-Naby et al., 2008). However, few studies have evaluated its potential for fluid infiltration and its role for transporting heat and matter into the Pan-African sequences.

In this article, we describe calc-silicates from Wadi Solaf in southern Sinai, Egypt which is one of the major basement complexes exhumed in association with the Najd fault system (Abu-Alam and Stüwe, 2009). We will first discuss field and petrological relationships, mineral chemistry and whole rock chemical variations as well as thermodynamic behaviour of the amphibolite facies calc-silicates and then use this information to place some constraints on the fluid evolution through the Najd fault system.

2. Geological setting and regional overview

The Wadi Feiran–Solaf metamorphic complex constitutes an elongated folded belt in southern Sinai that is about 40 km long and 5–11 km wide, trending NW–SE parallel to the orientation of the Najd fault system. It has evolved and was exhumed in close connection with the activity of this shear zone system (Abu-Alam and Stüwe, 2009). The complex can be divided into two zones: the Feiran zone in the northwest and the Solaf zone (Fig. 1) in the southeast. The Solaf zone is constituted mostly of quartzofelds-

* Corresponding author.
E-mail address: tamer.abu-alam@uni-graz.at (T.S. Abu-Alam).

1464-343X/$ - see front matter © 2010 Elsevier Ltd. All rights reserved.
doi:10.1016/j.jafrearsci.2010.05.004

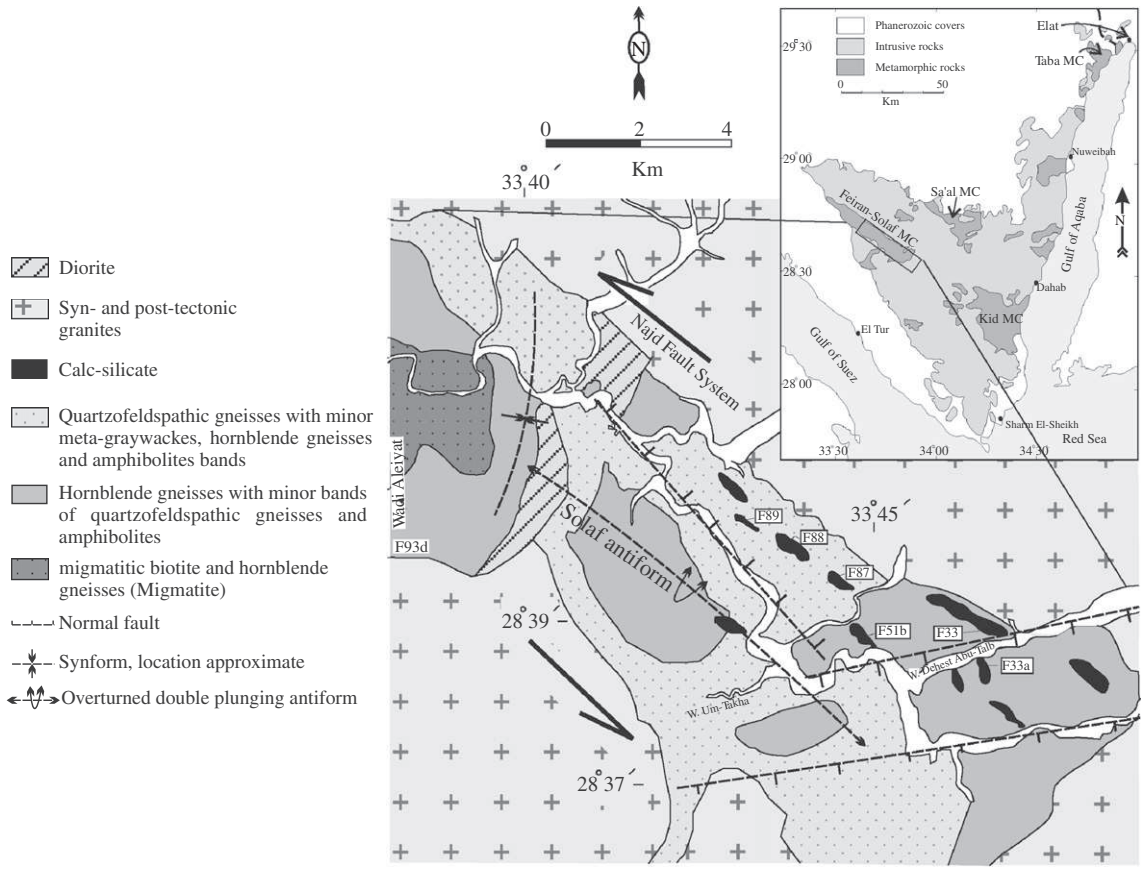

Fig. 1. Location and simplified geological map of the Solaf metamorphic complex after Abu-Alam and Stüwe (2009). Calc-silicate locations after Hashad et al. (2001). The white squares are the sample locations (F87, F88, F89, F51b, F33 and F33a). Lithological changes are often gradational and the mapped contacts are therefore approximate.

pathic gneisses and hornblende gneisses with mapable portions of calc-silicate rocks that do not occur in the Feiran zone. The rock units in the entire complex are systematically arranged around two doubly plunging antiformal structures: the NW plunging Feiran antiform and the SE plunging Solaf antiform. Both formed during an exhuming wrench phase of the orogen scale shear zone system. The calc-silicates generally appear to be located in the structurally highest levels (Fig. 2a).

Several authors have observed that metamorphic grade in the Feiran–Solaf metamorphic complex appears to increase towards the core of the structure, i.e. towards deeper structural levels in the center of the belt (Fig. 2a). In the center metamorphic grade is reported to have reached upper amphibolite facies and locally granulite facies conditions from 700 °C to 750 °C at pressure from 6 kbar to 8 kbar during the Pan-African Orogeny around 600 Ma (Akaad et al., 1967a,b; El-Gaby and Ahmed, 1980; Hashad et al., 2001; Eliwa et al., 2008; Abu-Alam and Stüwe, 2009). In contrast, the metamorphic grade of the rocks at higher structural level is reported to be around 600–650 °C at the same pressure condition (Abu-Alam and Stüwe, 2009).

The calc-silicates are exposed in the form of discontinuous lenses up to several hundreds of metres in size and thin bands up to metres in width, running parallel to and in contact with the granitoid rock at the outer most rim of the Solaf antiform (Figs. 1 and 2b). They are characterized by well developed reddish brown garnet crystals up to several centimetres in size (Fig. 2c). The calc-silicate rocks are fine grained, massive, light- to dark-green in colour and display spectacular folding on a centimetre and decimetre scale (Fig. 2c and d). They consist of calcite, garnet, wollastonite, clinopyroxene, anorthite, albite, clinozoisite, epidote, prehnite, vesuvianite, quartz and magnetite. Calc-silicates also contain minor marble bands.

The plutonic rocks in the study area are represented by syn- and post-tectonic granites and diorite. The syn-tectonic granitoid rocks intruded along the southern and eastern borders of the Solaf zone (in contact with the calc-silicate) in close temporal connection with the peak metamorphic events of the region around 632 ± 3 Ma (Stern and Manton, 1987). These granites were intruded at depth 9–20 km with wide range of temperature (588–795 °C) (Farahat et al., 2004, 2007; Helmy et al., 2004). The post-tectonic granites form large mountainous outcrops bordering the complex along the eastern and the southern parts of the Feiran zone but intruded postdate to the structural and metamorphic evolution of the region around 610–550 Ma (Stern and Hedge, 1985; Beyth et al., 1994) and are therefore of no relevance here. Granitic dykes, pegmatitic, quartz and k-feldspar-rich veins also cut the region. The paragneisses around these dykes are enriched in k-feldspar. Most of these dykes are parallel to the metamorphic foliation and to the Najd fault system trend (NW–SE).

The history of the Pan-African deformation in Sinai can be described in terms of four Proterozoic deformation phases D_1–D_4 (e.g. Eliwa et al., 2008; Abu-Alam and Stüwe, 2009), where D_1 formed the penetrative metamorphic foliation S_1 and stretching lineation L_1. The main metamorphic foliation (S_1) is parallel to the Najd fault system trend. Most high grade minerals grow in the lineation (L_1) suggesting that peak metamorphism was associated with this deformation event during an early Pan-African extensional environment. Abu-Alam and Stüwe (2009) show that there is also a pre-S_1 foliation preserved as an inclusion patterns in the high grade metamorphic minerals. The subsequent D_2 and D_3 phases formed folds

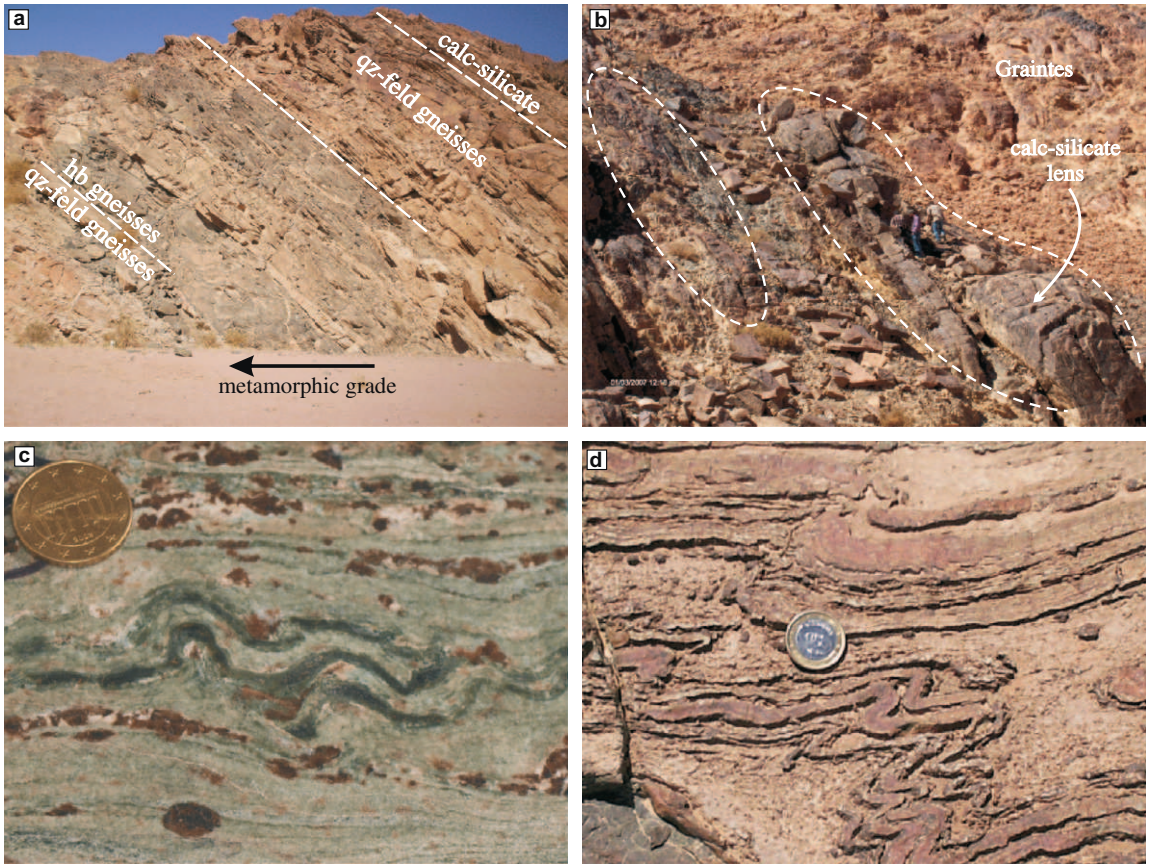

Fig. 2. Field photographs. (a) Interfingering and repetition between hornblende gneisses (hb gneisses) and quartz-feldspathic gneisses (qz-feld gneisses), the calc-silicate at the top of the succession. The arrow shows the increasing of the regional metamorphic grade. (b) Two calc-silicate discontinuous lenses running parallel to and in contact with the granitoid rocks (Wadi Dehest Abu-Talb). (c) Close up view showing folded pyroxene-wollastonite rich bands within the calc-silicate rocks. (d) Close up view showing highly folded garnet bands. There are alternative between calcite-rich softer bands and garnet bearing weathering resistant bands.

and occurred due to shortening in NE–SW direction. The D_3, phase is correlated with the sinistral NW–SE Najd fault system (El-Shafei and Kusky, 2003; Abu-Alam and Stüwe, 2009). Fowler and Hassan (2008) suggested that the major doubly plunging antiforms building the map scale geometry of the belt were formed during D_3 during the exhumation of the belt in the oblique transpressive regime of the Najd fault system (Abu-Alam and Stüwe, 2009). D_4 is a gentle warping event that domed up the entire belt.

3. Petrography

Calc-silicate rocks are divided into three groups. Groups CS_1 and CS_2 are mineralogically similar and differ only with respect to their state of deformation: CS_1 calc-silicates are highly deformed and CS_2 is largely un-deformed. Both CS_1 and CS_2 contain calcite, garnet, plagioclase, albite, wollastonite, clinopyroxene, quartz and k-feldspar as well as accessory apatite and sphene. Prehnite, vesuvi-

Table 1
Summary of the mineralogical composition and the textures of the studied calc-silicate samples.

Sample	Stable mineral											Metastable mineral	
	Calcite	Plag.	Alb	Py	Garnet	Epidote	wo	q	Preh.	Vesuv.	Sphene	Ksp	Magnetite
F88	in + m	in + m	in + m	in + m	p + m	in in preh.		in + m	in + m				
F87	m	in + m	m	m	m	m		m			m	m	p
F80	m	m	m	m	m	?		m			m	m	m
F81	in + m	in + m	in + m	in + m	p + m	m		in + m					
F89	in + m	m	in + m	in + m	p + m		in + m	in + m	in		in	in + m	
F33a	in + m	m	m	in + m	p + m		in + m	in			in	in + m	
F33	in + m	m	in + m	in + m	p + m		in + m	in + m				p + m	
F51b	in + m	in + m	in	in + m	p		in + m	m		in		in	
F51c	in + m	in + m	m	in + m	p		in + m	m				in	
F51a	in + m	m	in + m	in + m	p		in + m	in + m			m	in + m	
F51	in + m	in + m	?	in + m	p		in + m	in + m			m	in	
F33b	in + m	m	in + m	in + m	p + m		m	in + m			m	in	m

in – inclusion.
m – matrix.
p – porphyroblast.

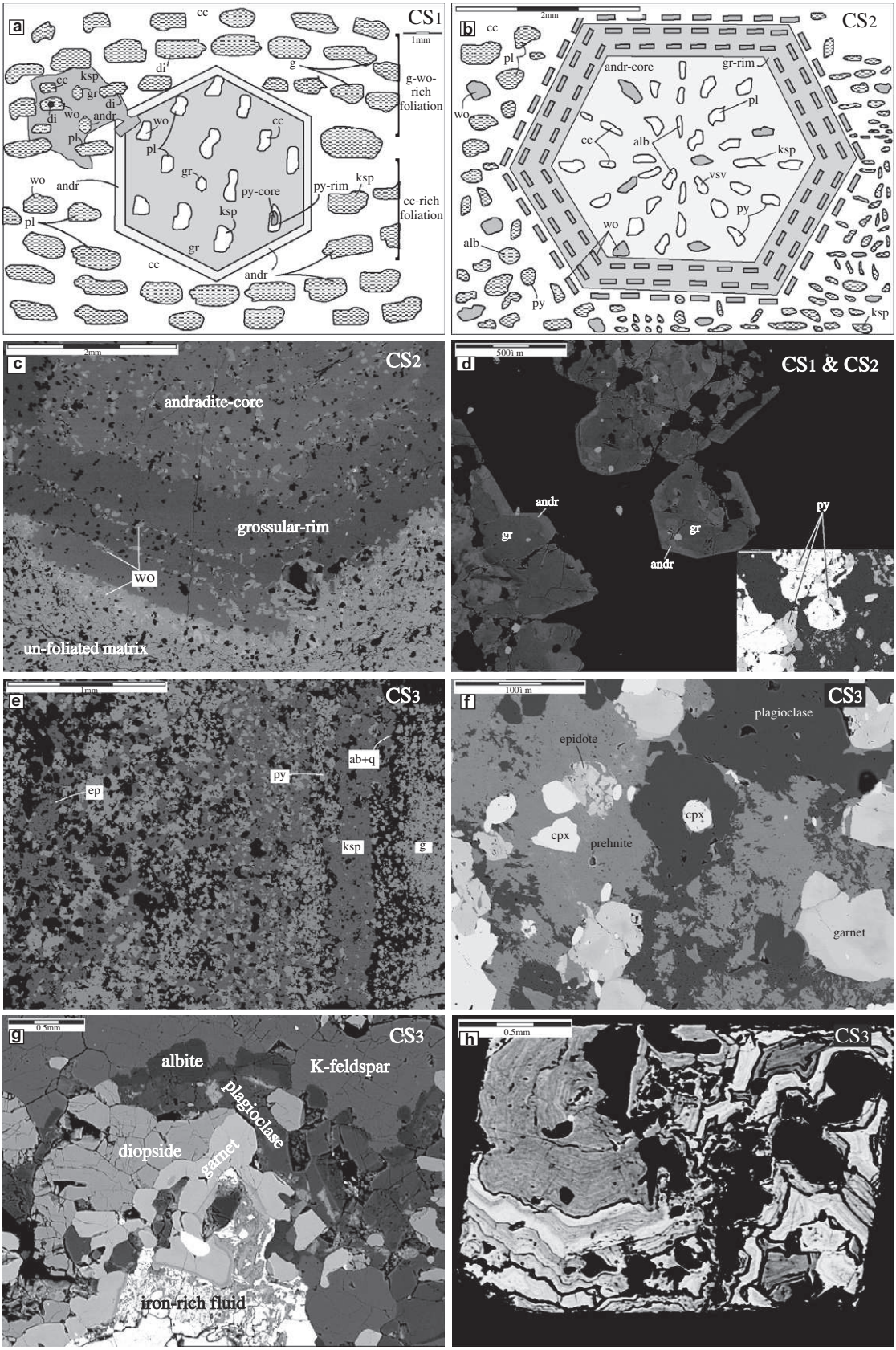

Fig. 3. Photomicrographs of the main rock types. (a) Sketch shows the main mineral relationships in the CS_1. (b) Sketch showing the idiomorphic garnet crystal grows over un-foliated matrix. The outer rim of the garnet crystal has concentric wollastonite inclusions. (c) Backscattered-electron image showing the spectacular concentric zoning growth of the wollastonite mineral in the garnet porphyroblasts as inclusions and around the porphyroblasts. (d) Andradite rims around euhedral grossular crystals. Note the garnet crystals contain clinopyroxene inclusions (bottom right backscattered image). (e) Fine-grained metamorphic foliation without porphyroblasts of CS_3 calc-silicate. (f) The prehnite grows statically and pervasively across the CS_3 calc-silicate and contains clinozoisite, epidote and garnet remnants. (g) Corona texture of different mineral zones around iron rich injected fluid (CS_3 calc-silicate). (h) Backscattered-electron image showing highly zoned magnetite crystal of CS_3 calc-silicate.

anite and magnetite are rare (Table 1). The main discerning feature of group CS_3 is the presence of clinozoisite/epidote.

In CS_1, garnet occurs as small euhedral crystals (0.2 × 0.3 mm) in the S_1 foliation but also as large idiomorphic porphyroblasts (4.5 × 5 mm) (Fig. 3a). Deformed garnet porphyroblasts are also present. The long axes of the deformed garnet crystals are parallel to the metamorphic foliation. These porphyroblasts contain mineral inclusions which are wollastonite, clinopyroxene, calcite, anorthite and albite. Minor quartz is also present. The metamorphic foliation (S_1) wrapping around the garnets is defined by a continuous foliation of calcite, plagioclase, albite, wollastonite, and clinopyroxene which define greenish weathering resistant bands up to 1–3 cm wide and which alternate with softer calcite rich layers (Fig. 2c and d). Calcites are colourless, euhedral to subhedral crystals with a perfect cleavage parallel to (1 0 1 1). The size of the calcite crystals ranges between 0.2 mm and 0.9 mm. Wollastonite and clinopyroxene are small crystals (0.1 × 0.2 mm). Two types of k-feldspar are present: small crystals in the metamorphic foliation and as large post-tectonic porphyroblasts.

In CS_2, garnet grows as large brown porphyroblasts in an un-deformed matrix (Fig. 3b and c). The size of these idiomorphic crystals is more or less the same as in CS_1 but the small garnet crystals are not present here. The garnet crystals contain mineral inclusion. These mineral inclusions are mainly wollastonite arranged in spectacular concentric growth zoning (Fig. 3c) but also clinopyroxene, calcite, anorthite, albite, quartz and k-feldspar. Minor prehnite and vesuvianite are also present as small inclusions (0.05 × 0.1 mm) usually concentrated in the center of garnet porphyroblasts. In particular vesuvianite generally occurs as well defined idiomorphic small inclusions possibly indicating that it was incorporated during the early stages of garnet growth. The matrix around these porphyroblasts consists mainly of wollastonite and calcite but clinopyroxene, plagioclase, albite, k-feldspar and quartz are also present. In both types of the calc-silicate (CS_1 and CS_2), garnet porphyroblasts are characterized by presence of concentric zonation. This zonation is defined by alternative light (andradite) and dark (grossular) bands. In addition the small grossular crystals are surrounded by andradite rims (Fig. 3d).

CS_3 calc-silicates are characterized by the presence of clinozoisite/epidote (Fig. 3e) and the absence of wollastonite as well as a pervasive late overgrowth of prehnite. Two types of garnet are present: small garnet crystals (0.2 × 0.4 mm) and large deformed garnet porphyroblasts (2.5 × 6 mm). Calcite, plagioclase, albite, pyroxene, clinozoisite, epidote and quartz are the main inclusion minerals within the deformed porphyroblasts. The metamorphic foliation (S_1) around the garnets is defined mainly by continuous foliation of clinozoisite, epidote, quartz and calcite. Clinopyroxene, plagioclase, albite and k-feldspar are also present in the metamorphic matrix (Fig. 3e). The prehnite grows statically and pervasively across the thin sections. Clinozoisite, epidote and garnet remnants are present within the prehnite (Fig. 3f). Characteristic corona textures are developed in the metamorphic foliation. This texture is defined by different mineral zones growing around an iron-rich phase (Fig. 3g). These mineral zones are garnet, clinopyroxene, plagioclase, albite and k-feldspar (from the inner to the outer zone). Few, euhedral magnetite porphyroblasts grow over the S_1 foliation. The magnetite porphyroblasts have a strong zonation (Fig. 3h).

4. Mineral chemistry

The minerals were analyzed at the Institute of Earth Science, Karl-Franzens-Universität Graz, Austria, with a JEOL JSM-6310 scanning electron microscope following standard procedures, operating in EDS/WDS mode at 5 nA beam current, accelerating voltage 15 kV and duration time is 100 s. The chemical formula of Tables 2–4 were calculated using the software AX (http://rock.esc.cam.ac.uk/astaff/holland/) and Norm (Ulmer, 1986) and are based on six oxygen atoms for pyroxene and wollastonite, 50 cations for vesuvianite, eight oxygen atoms for feldspars, 11 oxygen atoms and ignoring H_2O for prehnite, 12.5 oxygen atoms for clinozoisite/epidote, 12 oxygen atoms for garnet and 12 oxygen atoms and ignoring H_2O for hydrogarnet. AX (and the activity models implemented therein) was also use to calculate the end-member activities cited below. For vesuvianite and prehnite activity was assumed to be ideal. The site distribution of vesuvianite is after Hoisch (1985 and references therein). The mineral abbreviations which will be used in the following sections are from Holland and Powell (1998).

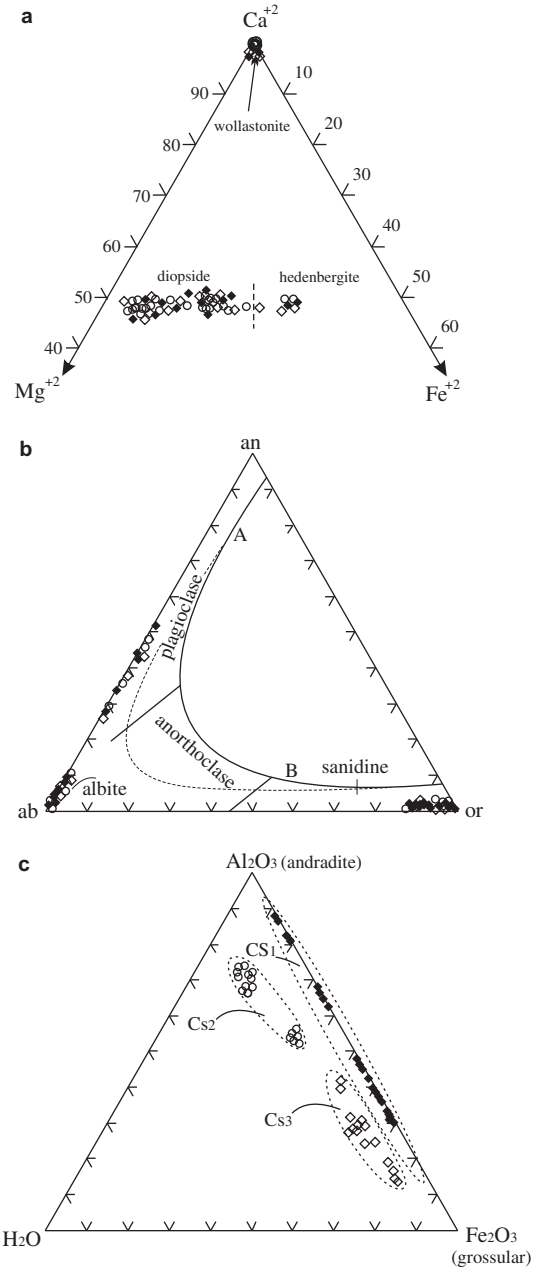

Fig. 4. Mineral chemistry. (a) Ca^{+2}–Mg^{+2}–Fe^{+2} ternary diagram showing the variation in pyroxene chemistry and the pure composition of the wollastonite. (b) an-ab-or ternary diagram showing the feldspar composition of different calc-silicate samples. AB curve is the limit of ternary solid solution after Deer et al. (1992). (c) Al_2O_3–Fe_2O_3–H_2O ternary diagram showing the two solid solution series of garnet mineral: andradite–grossular solid solution and hydroandradite–hydrogrossular solid solution. Black rhomb is CS_1, circle is CS_2 and white rhomb is CS_3.

Table 2
Representative mineral analyses of CS_1 calc-silicate. The chemical formula, Fe_2O_3, FeO and the end-member activities were calculated using the software AX and Norm and are based on number of oxygen atoms that cited in the text. Mineral abbreviations are after Holland and Powell (1998). The b.d.l is below detection limit.

Mineral sample	CS_1-cpx				CS_1-wo		CS_1-feldspar					CS_1-garnet									
	f33a		f33		f33	f33a	f33a			f33		f33a					f33				
												Core			Rim		Porphyroblast			Matrix	
SiO_2	52.30	53.08	51.68	52.48	51.36	50.89	64.35	68.97	68.60	64.82	69.91	37.12	37.67	38.81	38.97	38.07	36.62	37.17	37.60	36.29	36.29
TiO_2	0.06	0.05	0.15	0.16	b.d.l.	b.d.l.	0.30	b.d.l.	0.09	0.33	b.d.l.	0.82	0.80	0.78	0.11	1.29	0.57	0.52	0.51	0.52	0.92
Al_2O_3	1.67	1.04	1.29	0.22	b.d.l.	0.08	18.34	19.62	19.56	18.70	19.67	10.29	12.61	19.84	21.06	15.06	8.61	11.84	12.12	8.99	8.34
Fe_2O_3	–	–	–	–	–	–	0.06	0.03	0.02	–	–	15.57	13.62	3.05	2.94	9.13	18.88	14.43	14.09	18.78	19.32
FeO	6.22	3.81	12.35	10.67	0.14	0.15	–	–	–	b.d.l.	b.d.l.	0.27	–	–	–	–	0.01	–	–	–	–
MnO	0.61	0.62	0.72	0.75	0.35	0.39	0.02	b.d.l.	b.d.l.	b.d.l.	b.d.l.	0.59	0.33	0.14	0.25	0.43	0.61	0.24	0.33	0.19	0.28
MgO	13.79	15.60	9.63	10.93	b.d.l.	0.03	0.12	0.11	b.d.l.	0.41	0.28	0.31	0.52	0.51	0.56	0.64	0.10	0.04	b.d.l.	b.d.l.	0.06
CaO	24.86	25.25	24.53	25.09	48.34	48.39	0.11	0.13	0.38	0.17	0.10	34.04	35.03	36.01	36.38	35.63	33.95	35.13	35.19	34.56	34.80
Na_2O	0.57	0.45	0.36	0.20	b.d.l.	0.02	0.36	11.37	11.47	0.75	11.98	b.d.l.	b.d.l.	b.d.l.	b.d.l.	b.d.l.	b.d.l.	b.d.l.	b.d.l.	b.d.l.	b.d.l.
K_2O	b.d.l.	b.d.l.	b.d.l.	b.d.l.	b.d.l.	b.d.l.	16.34	0.04	0.07	15.50	0.03	0.03	0.01	b.d.l.	b.d.l.	b.d.l.	b.d.l.	b.d.l.	b.d.l.	b.d.l.	b.d.l.
Total	100.01	100.00	100.71	100.53	100.20	100.07	100.02	100.26	100.17	100.71	102.00	99.05	100.60	99.14	100.26	100.24	99.35	99.37	99.97	99.33	100.01
O	6	6	6	6	6	6	8	8	8	8	8	12	12	12	12	12	12	12	12	12	12
Si	1.932	1.942	1.960	1.980	1.990	1.977	2.980	2.998	2.990	2.970	2.992	2.968	2.965	2.972	2.966	2.966	2.980	2.980	2.980	2.960	2.950
Ti	0.002	0.001	–	–	–	–	0.010	–	0.003	0.010	–	0.050	0.047	0.045	0.006	0.075	0.030	0.030	0.030	0.030	0.060
Al	0.073	0.045	0.060	0.010	–	0.004	1.001	1.005	1.005	1.010	0.993	0.970	1.170	1.790	1.889	1.383	0.820	1.120	1.130	0.860	0.800
Fe^{+3}	0.099	0.097	0.040	0.040	–	–	0.002	0..1	0.001	–	0.003	0.997	0.807	0.176	0.168	0.535	1.150	0.870	0.840	1.150	1.180
Fe^{+2}	0.093	0.020	0.350	0.300	–	0.005	–	–	–	–	–	0.018	–	–	–	–	–	–	0.010	–	–
Mn	0.019	0.019	0.020	0.020	0.010	0.013	0.001	–	–	–	–	0.040	0.022	0.009	0.016	0.028	0.040	0.020	0.020	0.010	0.020
Mg	0.760	0.851	0.540	0.620	–	0.002	0.008	0.007	–	0.030	0.018	0.037	0.061	0.058	0.064	0.074	0.010	–	–	–	0.010
Ca	0.984	0.990	1.000	1.010	2.010	2.014	0.005	0.006	0.018	0.010	0.005	2.917	2.954	2.954	2.967	2.974	2.960	3.010	2.990	3.020	3.030
Na	0.041	0.032	0.030	0.020	–	0.001	0.032	0.958	0.970	0.070	0.994	–	–	–	–	0.001	–	–	–	–	–
K	–	–	–	–	–	–	0.965	0.002	0.004	0.910	0.002	0.003	0.001	–	–	–	–	–	–	–	–
di	0.760	0.850	0.570	0.650																	
hed	0.125		0.420	0.390																	
an									0.031												
ab							0.227	0.990	0.980	0.447	0.990										
san							0.960			0.930											
gr												0.200	0.300	0.760	0.830	0.430	0.150	0.310	0.310	0.180	0.160
andr												0.240	0.160	0.007	0.004	0.081	0.330	0.190	0.180	0.310	0.350

Table 3
Representative mineral analyses of CS_2 calc-silicate.

Mineral sample	CS_2-cpx				CS_2-wo		CS_2-feldspar					CS_2-garnet						CS_2-vesuvenite		
	F51b		F89		F51b	F89	F51b		F89			F51b			F89			F51b		
												Porphyroblast			Core		Rim			
SiO_2	51.86	51.98	55.45	53.28	50.47	51.49	68.49	60.27	65.61	71.23	65.98	35.84	36.05	36.01	36.69	36.78	37.10	36.24	35.94	36.14
TiO_2	b.d.l.	0.04	0.01	0.15	0.01	0.10	b.d.l.	b.d.l.	0.05	0.02	0.15	0.56	0.56	0.51	1.34	1.27	0.57	3.49	3.67	3.28
Al_2O_3	0.77	0.80	0.69	0.64	0.28	0.01	20.24	23.88	18.14	19.52	18.82	15.29	15.44	15.71	17.39	17.71	18.49	14.04	13.99	14.62
Fe_2O_3	–	–	–	–	–	–	–	–	–	–	–	9.37	9.69	9.26	3.96	3.70	2.90	–	–	–
FeO	7.58	7.25	1.43	7.10	0.12	0.11	b.d.l.	b.d.l.	b.d.l.	b.d.l.	b.d.l.	–	–	–	–	–	–	3.46	3.82	3.56
MnO	0.53	0.51	0.26	0.66	0.28	0.28	b.d.l.	0.02	b.d.l.	0.03	b.d.l.	0.25	0.25	0.24	0.33	0.40	0.42	0.38	0.28	0.46
MgO	13.00	12.99	16.10	12.11	0.03	b.d.l.	0.05	0.23	b.d.l.	b.d.l.	0.23	0.22	0.31	0.34	0.56	0.64	0.38	2.21	2.06	1.82
CaO	24.71	24.98	26.18	24.98	48.70	48.02	0.94	6.04	0.37	0.11	0.26	34.19	34.21	34.14	35.52	35.49	35.66	35.70	35.41	35.61
Na_2O	0.33	0.34	0.26	0.29	0.01	b.d.l.	10.97	8.34	0.21	11.76	0.93	b.d.l.	b.d.l.	b.d.l.	b.d.l.	0.04	0.01	0.30	0.29	0.21
K_2O	b.d.l.	b.d.l.	b.d.l.	0.01	0.02	b.d.l.	0.02	0.19	16.39	b.d.l.	15.36	b.d.l.	b.d.l.	b.d.l.	b.d.l.	0.01	b.d.l.	b.d.l.	0.01	b.d.l.
F	b.d.l.	b.d.l.	b.d.l.	b.d.l.	b.d.l.	b.d.l.	b.d.l.	b.d.l.	b.d.l.	b.d.l.	b.d.l.	b.d.l.	b.d.l.	b.d.l.	b.d.l.	b.d.l.	b.d.l.	2.05	2.33	2.14
Cl	b.d.l.	b.d.l.	b.d.l.	b.d.l.	b.d.l.	b.d.l.	b.d.l.	b.d.l.	b.d.l.	b.d.l.	b.d.l.	b.d.l.	b.d.l.	b.d.l.	b.d.l.	b.d.l.	b.d.l.	0.32	0.53	0.31
[a]H_2O	0.0	0.0	0.0	0.0	0.0	0.0	0.0	0.0	0.0	0.0	0.0	4.28	3.49	3.79	4.21	3.96	4.47	1.67	1.47	1.62
Total	98.94	98.83	100.41	99.21	100.00	100.01	100.75	99.07	100.79	102.76	101.81	100.00	100.00	100.00	100.00	100.00	100.00	99.86	99.80	99.77
O	6	6	6	6	6	6	8	8	8	8	8	12	12	12	12	12	12	73	73	73
Si	1.954	1.958	2.006	2.004	1.965	1.994	2.965	2.707	3.009	3.020	2.984	2.938	2.930	2.932	2.922	2.918	2.949	17.968	17.911	17.954
Ti	–	0.001	–	0.004	–	0.003	–	–	0.002	0.001	0.005	0.034	0.034	0.031	0.080	0.076	0.034	1.298	1.374	1.225
Al	0.034	0.036	0.029	0.028	0.013	–	1.033	1.265	0.981	0.976	1.004	1.477	1.479	1.507	1.633	1.656	1.732	8.205	8.217	8.558
Fe^{+3}	0.076	0.069	–	–	–	–	0.008	0.005	–	–	–	0.578	0.593	0.567	0.237	0.221	0.173	1.529	1.499	1.264
Fe^{+2}	0.163	0.159	0.043	0.223	0.004	0.004	–	–	–	–	–	–	–	–	–	–	–	–	0.171	0.303
Mn	0.017	0.016	0.008	0.021	0.009	0.009	–	0.001	–	0.001	–	0.018	0.017	0.017	0.022	0.027	0.028	0.162	0.119	0.190
Mg	0.730	0.730	0.868	0.679	0.002	–	0.003	0.015	–	–	0.015	0.027	0.038	0.041	0.067	0.076	0.046	1.632	1.530	1.349
Ca	0.997	1.008	1.014	1.007	2.031	1.993	0.044	0.291	0.018	0.005	0.013	3.003	2.979	2.978	3.031	3.017	3.036	18.967	18.905	18.951
Na	0.024	0.025	0.018	0.021	–	–	0.921	0.726	0.019	0.967	0.081	–	–	0.001	–	0.06	–	0.282	0.275	0.207
K	–	–	–	–	–	–	0.001	0.011	0.959	–	0.887	–	–	–	–	0.001	–	–	0.004	–
F	–	–	–	–	–	–	–	–	–	–	–	–	–	–	–	–	–	3.219	3.679	3.360
Cl	–	–	–	–	–	–	–	–	–	–	–	–	–	–	–	–	–	0.266	0.452	0.261
H	–	–	–	–	–	–	–	–	–	–	–	–	–	–	–	–	–	5.515	4.870	5.379
di	0.740	0.740	0.880	0.700																
hed	0.220	0.220	0.068	0.300																
an			0.081	0.066			0.079	0.470												
ab							0.950	0.710	0.137	0.990	0.529									
san									0.960		0.910									
gr												0.520	0.510	0.520	0.690	0.700	0.790			
andr												0.066	0.065	0.059	0.018	0.016	0.009			
vsv																		0.370	0.303	0.310

[a] H_2O for garnet = 100 − ∑ of other oxides.

Table 4
Representative mineral analyses of CS_3 calc-silicate.

Mineral sample	CS_3-cpx				CS_3-feldspar					CS_3-garnet				CS_3-epidote				CS_3-prehnite		CS_3-Fe-phase	
	F88		F87		F88		F87			F88		F87		F88		F87		F88		F87	
										Porphyroblast	Matrix	Porphyroblast									
SiO_2	52.04	52.66	53.21	53.42	70.22	56.93	62.78	70.64	65.84	34.19	34.89	35.31	35.75	38.80	37.90	37.19	37.43	43.97	44.29	5.62	0.36
TiO_2	0.05	b.d.l.	0.01	0.06	b.d.l.	b.d.l.	b.d.l.	0.03	0.06	0.74	0.70	0.57	0.48	0.01	0.05	0.09	0.11	b.d.l.	b.d.l.	0.02	0.08
Al_2O_3	0.49	0.45	0.17	0.45	19.19	27.94	22.45	18.74	17.18	7.48	7.59	4.80	5.73	25.61	25.17	23.98	24.42	23.28	23.55	0.28	0.36
Fe_2O_3	–	–	–	–	–	–	0.03	0.11	0.22	19.76	19.64	23.11	21.31	6.63	7.13	12.50	10.87	0.84	0.19	45.76	67.70
FeO	12.05	11.66	9.48	9.83	b.d.l.	b.d.l.	–	–	–	–	–	1.46	2.72	2.68	2.69	–	–	–	–	32.02	31.23
MnO	1.05	1.01	0.84	0.88	0.04	b.d.l.	b.d.l.	b.d.l.	b.d.l.	0.60	0.55	0.73	0.48	0.19	0.23	0.08	0.30	0.04	0.12	0.09	b.d.l.
MgO	8.99	9.75	11.34	11.19	b.d.l.	0.41	0.01	b.d.l.	b.d.l.	0.20	b.d.l.	b.d.l.	0.11	0.33	0.27	b.d.l.	0.27	b.d.l.	b.d.l.	0.07	b.d.l.
CaO	24.74	24.55	24.67	24.96	0.47	10.86	7.95	0.46	0.17	33.44	34.22	31.65	31.05	23.78	23.62	23.77	23.60	27.25	27.45	0.94	0.22
Na_2O	0.19	0.33	0.18	0.13	11.01	5.47	8.64	11.84	1.12	b.d.l.	0.01	b.d.l.	b.d.l.	0.01	0.05	0.02	0.02	0.04	0.06	0.11	0.04
K_2O	0.06	b.d.l.	b.d.l.	b.d.l.	0.06	0.20	0.08	b.d.l.	15.77	0.04	0.06	b.d.l.	b.d.l.	0.05	b.d.l.	b.d.l.	b.d.l.	b.d.l.	b.d.l.	0.05	b.d.l.
H_2O[a]	–	–	–	–	–	–	–	–	–	3.55	2.34	2.36	2.30	1.91	2.89	1.85	1.88	4.34	4.36	–	–
Total	99.69	100.44	99.90	100.95	101.10	101.81	101.94	101.81	100.36	100.00	100.00	100.00	100.00	99.56	99.69	99.56	98.90	99.77	100.08	85.02	100
O	6	6	6	6	8	8	8	8	8	12	12	12	12	12.5	12.5	12.5	12.5	11	11	4	4
Si	1.999	2.000	2.009	2.000	3.023	2.510	2.756	3.029	3.032	2.875	2.896	2.988	3.009	3.054	3.024	2.967	2.989	3.035	3.044	0.245	0.014
Ti	0.001	–	–	–	–	–	–	0.001	0.002	0.047	0.044	0.037	0.030	–	0.003	0.005	0.007	–	–	0.001	0.002
Al	0.022	0.020	0.008	0.020	0.974	1.452	1.161	0.947	0.932	0.742	0.743	0.479	0.568	2.377	2.368	2.255	2.299	1.894	1.907	0.015	0.016
Fe+3	–	0.002	–	–	0.003	0.015	0.001	0.004	0.008	1.251	1.227	1.472	1.350	0.393	0.428	0.750	0.653	0.048	0.004	1.504	1.953
Fe^{+2}	0.39	0.368	0.299	0.308	–	–	–	–	–	–	–	0.103	0.192	0.176	0.179	–	–	–	–	1.169	1.001
Mn	0.03	0.032	0.027	0.028	0.001	–	–	–	–	0.043	0.039	0.052	0.034	0.012	0.016	0.005	0.018	0.002	0.011	0.003	–
Mg	0.52	0.552	0.638	0.624	–	0.027	0.001	–	–	0.025	–	–	0.013	0.038	0.032	–	0.032	–	–	0.005	–
Ca	1.02	0.999	0.998	1.001	0.021	0.513	0.374	0.021	0.008	3.014	3.044	2.869	2.800	2.006	2.020	2.032	2.019	2.015	2.021	0.044	0.009
Na	0.01	0.024	0.013	0.009	0.919	0.468	0.735	0.984	0.100	–	0.002	–	–	0.007	0.007	–	0.003	0.005	0.008	0.009	0.003
K	–	–	–	–	0.003	0.011	0.004	–	0.927	0.004	0.006	–	–	0.001	–	0.002	–	–	–	0.003	–
H	–	–	–	–	–	–	–	–	–	–	–	–	–	1.00	1.00	1.00	1.00	2.00	2.00	–	–
di	0.550	0.580	0.660	0.650																	
hed	0.480	0.450	0.370	0.380																	
an					0.040	0.730	0.550	0.037													
ab					0.970	0.550	0.670	0.980	0.599												
san									0.910												
gr										0.130	0.140	0.036	0.041								
andra										0.400	0.410	0.530	0.460								
cz														0.610	0.570	0.270	0.295				
ep														0.390	0.420	0.700	0.653				
pre																		0.971	0.986		

[a] H_2O for garnet = 100 − ∑ of other oxides.

Pyroxenes include Fe–Mg clinopyroxenes and wollastonite and have similar chemical characteristics in all three groups of calc-silicates. Clinopyroxenes are zoned: cores are Mg-rich diopside with X_{Mg} = Mg/(Mg + Fe) = 0.68–0.98 and the Fe content increases towards the rims. The outer rims occasionally reach a chemical composition of hedenbergite (Fig. 4a) with X_{Mg} = 0.68–0.98. The activity of diopside (as calculated with AX) ranges between 0.49 and 0.88 while it is 0.12–0.54 for hedenbergite (Tables 2–4). The wollastonite is a pure Ca–Si bearing phase with negligible substitution of Ca^{+2} by Fe^{+2}, Mn^{+2} and Mg^{+2} and Si^{+4} by Ti^{+4} and Al^{+4} (Fig. 4a).

Feldspar includes both plagioclase and k-feldspar, also in all three types of calc-silicate. Plagioclase has a compositional range between pure albite and labradorite (Fig. 4b) with X_{Ca} = Ca/(Ca + Na + K) = 0.01–0.62. Activity of the end members in the albite–anorthite series is for albite: 0.13–0.99 and for anorthite: 0.02–0.73. The activities of albite and sanidine in potassium feldspars are 0.09–0.58 and 0.71–0.99, respectively.

Garnet chemistry shows that there are two solid solution series: andradite–grossular solid solution and hydroandradite–hydrogrossular solid solution (Fig. 4c). Element distribution maps (Fig. 5a and b) reveal compositional variation across the zoned garnet crystals in Al_2O_3 and FeO_{tot} (Fe_2O_3) which indicates that there is ionic substitution between Al^{+3} and Fe^{+3} in both series (Fig. 4c). Garnet composition of the CS_2 and the CS_3 is hydroandradite and hydrogrossular while the composition of CS_1 garnet is andradite-grossular (Tables 2–4). For both series, the garnet has X_{Ca} = Ca/(Ca + Mg + Fe) = 0.93–1. The activity of vesuvianite was calculated to be ideal and it ranges between 0.24 and 0.37.

Epidote is essentially a clinozoisite–epidote solid solution with clinozoisite activity in the range of 0.21–0.61 and epidote activity between 0.42 and 0.73 (Table 4). The activity of prehnite is in range 0.97 and 0.99. Scanning electron microscope images (Fig. 3h) reveal compositional variation across the zoned magnetite crystals; the lightest gray colour represents a pure magnetite composition

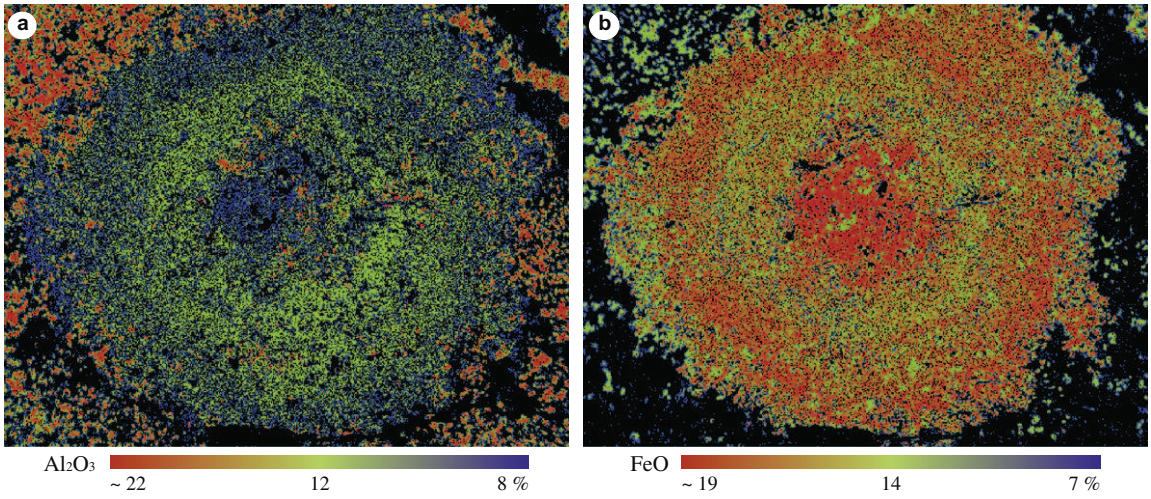

Fig. 5. Element distribution maps show the Al_2O_3 (a) and FeO (b) zonation in garnet porphyroblast. Note the garnet core and rim have andradite composition while the middle zone has a grossular composition.

Table 5
Representative XRF analyses of different calc-silicate groups; major elements in wt.%, trace elements (ppm).

Sample	CS_1						CS_2			CS_3		
	F33	F81	F33a	F80	F51a	F33b	F51b	F89	F51c	F51	F87	F88
SiO_2	50.49	49.66	47.23	49.42	44.51	53.83	40.80	46.62	40.59	49.35	57.59	50.25
Al_2O_3	11.00	9.37	8.97	9.72	9.32	9.91	4.21	4.10	4.20	13.00	13.60	14.12
Fe_2O_3	4.82	4.46	4.00	3.61	4.59	4.09	0.93	0.90	0.93	5.74	6.08	8.01
MnO	0.27	0.26	0.34	0.30	0.34	0.27	0.21	0.26	0.21	0.39	0.23	0.36
MgO	1.93	1.97	1.51	1.39	1.85	2.07	1.24	1.06	1.36	2.84	2.00	2.07
CaO	24.51	27.25	32.61	29.57	32.08	23.87	37.55	39.66	37.23	19.99	11.04	19.52
Na_2O	1.95	0.84	0.50	1.28	0.56	2.63	1.06	0.19	1.26	1.38	2.34	2.02
K_2O	1.63	3.34	1.97	1.80	1.78	1.92	0.70	1.55	0.64	4.05	4.54	0.63
TiO_2	0.41	0.29	0.33	0.33	0.33	0.40	0.17	0.16	0.17	0.51	0.41	0.61
P_2O_5	0.14	0.11	0.12	0.14	0.13	0.16	0.04	0.04	0.07	0.14	0.13	0.19
LOI	1.91	1.28	1.41	1.33	3.00	1.33	12.21	4.24	13.18	1.17	0.61	1.16
Sum	99.26	99.11	99.22	99.07	98.74	100.58	99.28	98.98	99.90	99	98.85	99.11
Ba	314	709	464	660	617	350	101	532	116	600	802	125
Ce	33	32	40	59	21	44	27	40	<30	31	21	34
Cr	30	25	28	21	38	31	25	25	21	37	<20	21
Ni	35	42	37	24	35	32	<20	<20	<20	63	38	36
Rb	36	77	41	51	44	42	<20	43	<20	86	104	26
Sr	83	174	131	297	256	133	378	403	371	494	187	243
V	72	28	36	37	61	67	40	34	50	80	40	89
Y	27	26	23	27	22	27	<20	<20	<20	37	37	31
Zn	202	131	107	91	99	206	26	24	27	136	77	115
Zr	102	119	90	143	114	109	59	54	49	198	177	191

while the darkest gray zones represent magnetite with silica component (Table 4). Calcite and quartz are virtually pure phases.

5. Whole rock geochemistry

The bulk rock chemistry of the calc-silicates was analyzed at the Institute of Earth Science, Karl-Franzens-Universität Graz, Austria, using a Bruker Pioneer S4 X-ray fluorescence spectrometer. Samples were prepared as fused pellets using $Li_2B_4O_7$ flux. Results of the whole rock analysis are shown in Table 5. It may be seen that the three groups of calc-silicates are also reflected in the whole rock chemistry (Fig. 6). For example, CS_2 samples have the lowest values for all the major oxides except CaO, probably simply reflecting a somewhat higher proportion of calcite in this group.

In order to test the rocks for fluid infiltration, several characteristic mobile and immobile elements were plotted against Al_2O_3,

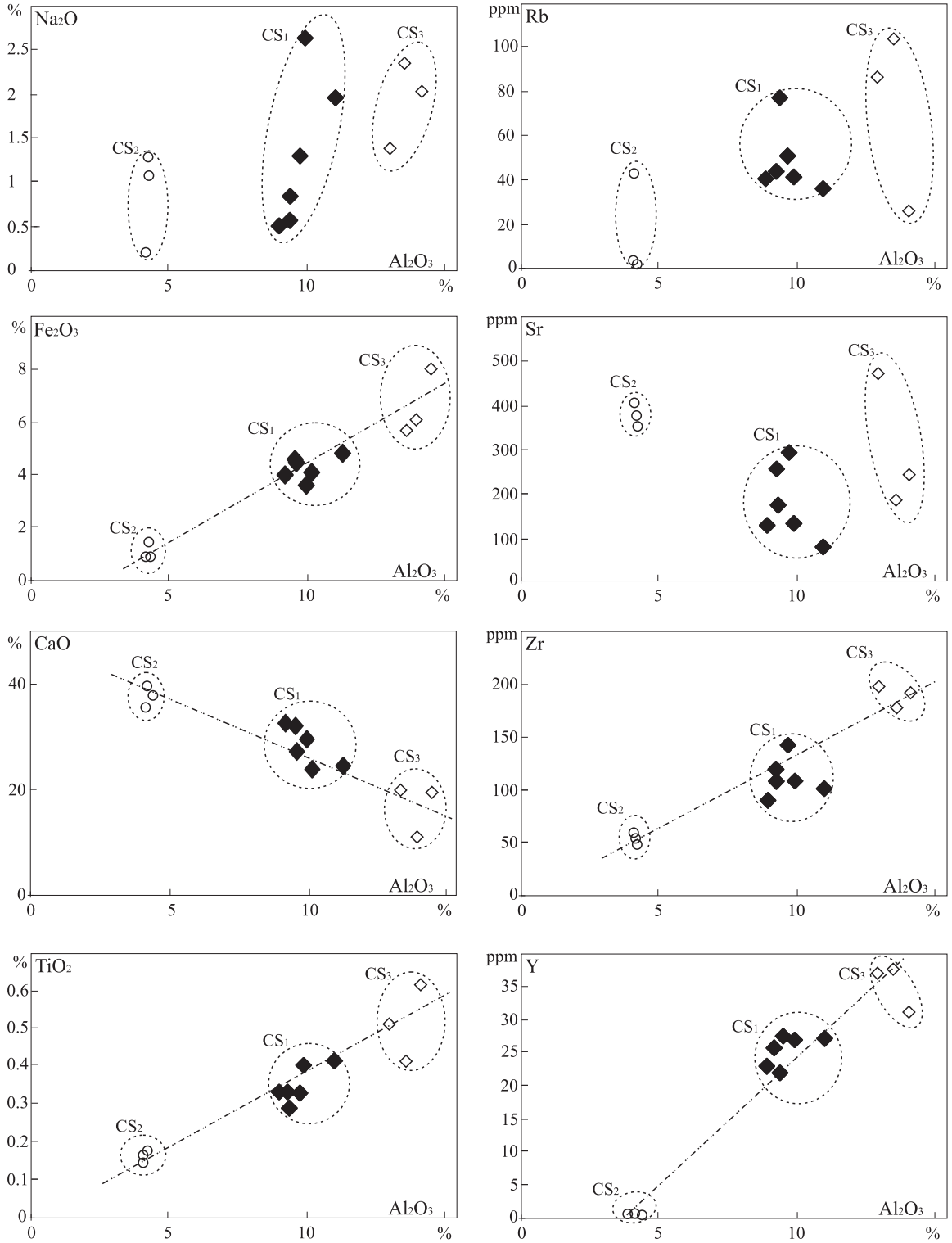

Fig. 6. Discrimination diagrams showing the chemical difference between the three calc-silicate groups. Black rhomb is CS_1, circle is CS_2 and white rhomb is CS_3.

which is generally considered to be immobile (e.g. Grant, 2005). Amongst the major elements Na_2O, CaO and – to some extent – Fe_2O_3 are considered mobile elements. Fig. 6 shows that there is a positive correlation between Al_2O_3 and Na_2O as well as between Al_2O_3 and Fe_2O_3 from CS_2 through CS_1 to CS_3 possibly suggesting that CS_3 was most influenced by fluid flow. However a positive correlation is also reflected in the correlation of the immobile TiO_2 with Al_2O_3. Only CaO has a negative correlation with Al_2O_3 which is interpreted in terms of the calcite content of the rocks (see above). Among the trace element there is also a positive correlation with Al_2O_3 regardless of the fact whether the chosen element is considered immobile (i.e. Zr) or mobile (e.g. Rb, Sr, Y).

6. Discussion

Mineral textures, equilibrium–disequilibrium phases and the fluid composition during peak metamorphism will be discussed in the following sections based upon the petrography, the mineral chemistry and the whole rock geochemistry. In the absence of any appropriate thermobarometer applicable to the calc-silicate rocks, the *PT* path of Abu-Alam and Stüwe (2009) will be used as a basis for this discussion. Their *PT* path was mainly constrained on the basis of metagraywackes on the same structural level as the calc-silicates. This *PT* path indicates a single-clockwise metamorphic cycle with peak conditions around 7–8 kbar and 650–700 °C. Following peak metamorphism the rocks were subjected to exhumation from the peak pressure to 4.8–5.3 kbar with only limited cooling to 645–685 °C. Finally, the Feiran–Solaf area cooled isobarically at this pressure to 475–525 °C.

In order to interpret the metamorphic reactions of the calc-silicates in *T*-XCO_2 space, a petrogenetic grid was calculated at pressure 7 kbar. THERMOCALC tc330 (Powell and Holland, 1988) and internally consistent dataset of Holland and Powell (1998) were used to construct the *T*-XCO_2 relationships. The simplified MCASH-CO_2 system (MgO–CaO–Al_2O_3–SiO_2–H_2O–CO_2) was used for constructing this section. These components constitute about 85% of the whole rock analysis. The grid was calculated for the phases wollastonite, grossular, anorthite, calcite, clinozoisite and quartz in presence of H_2O and CO_2. The grid was also tested for the stability of vesuvianite, but this phase is stable at high *T* and very low XCO_2 outside the region shown in Fig. 7. The *T*-XCO_2 grid (Fig. 7) is characterized by the presence of two invariant points: a wollastonite absent invariant point at 714 °C and XCO_2 = 0.124 and a clinozoisite absent invariant point at 803 °C and XCO_2 = 0.269. Because of the absence of clinozoisite from CS_1 and CS_2 calc-silicates, these rocks are likely to have formed around the clinozoisite invariant point. Correspondingly, the CS_3 calc-silicate formed around wollastonite invariant point due to the absence of the wollastonite.

6.1. Interpreted equilibrium and disequilibrium parageneses

The presence of inclusion phases within the garnet porphyroblasts constraints the origin of these porphyroblasts. Fig. 7 shows that garnet may be produced along five reactions: gr + q = wo + an (1); cc + wo + an = gr + CO_2 (2); cc + an + q = gr + CO_2 (3); zo + q = an + gr + H_2O (4) and cc + zo + q = gr + CO_2 + H_2O (5). However, only reactions (3), (4) and (5) are able to produce garnet porphyroblasts during prograde metamorphism because reaction (1) produces garnet but only during cooling, while reaction (2) is insensitive to temperature variation. For CS_1 and CS_2 clinozoisite bearing reactions are excluded and only reactions (3) is therefore likely to be responsible for garnet porphyroblasts growth. For CS_3, the wollastonite bearing reactions are excluded so that reactions (3), (4) and (5) may have produced garnet porphyroblasts.

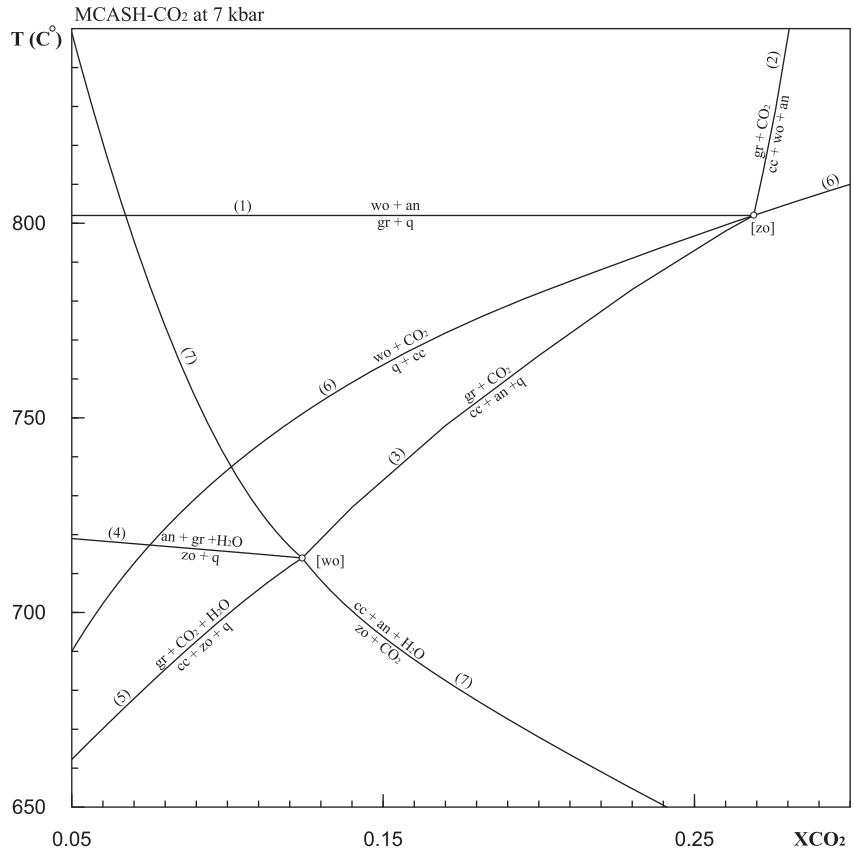

Fig. 7. *T*-XCO_2 grid in the system MCASH-CO_2 showing clinozoisite, wollastonite invariant points and different mineral reactions which are discussed in the text.

In CS_1 and CS_2, the presence of wollastonite-rich matrix around garnet porphyroblasts indicates that this matrix formed due to the reactions (1) and (2) or reaction (6): q + cc = wo + CO_2. As garnet porphyroblasts and the wollastonite in the matrix are stable together (Fig. 3b and c), reactions (1) and (2) are excluded and only reaction 6 is interpreted as the principal wollastonite producing reaction. In CS_3, the presence of clinozoisite-rich matrix (together with quartz, anorthite and garnet) indicates that this matrix is likely to have formed below reaction (4).

The presence of early vesuvianite as small inclusions within the garnet porphyroblasts of sample F51b (CS_2) may indicate that this phase formed as a result of one of the following reactions: vsv + wo + CO_2 = cc + di + gr + H_2O (8) and/or cc + di + an + gr + - H_2O = vsv + CO_2 (9). Both of these reactions occur at XCO_2 = 0.01–0.06 and in a temperature range of 580–850 °C outside the region of Fig. 7 and may indicate very low XCO_2 during the early stages of the evolution.

Late stage overprint in CS_3 calc-silicates is identified by the presence of prehnite mineral grown statically and pervasively across the thin sections. Texturally, the prehnite was formed due to the consumption of grossular and clinozoisite. The following reaction is suggested to explain the formation of this low-grade mineral: pre = gr + zo + q + H_2O (10). This reaction was tested using THERMOCALC at 5 kbar (isobaric cooling pressure). The prehnite phase may have formed at temperature 311–296 °C and XCO_2 = 0.05–0.4.

Two types of the k-feldspar were recognized; small crystals as bands parallel to the metamorphic foliation in CS_3 and as large post-tectonic porphyroblasts in CS_2. Abu-Alam and Stüwe (2009) suggested that the k-feldspar in the hornblende gneisses and in the quartzofeldspathic gneisses (the same structural level of the calc-silicate) is in disequilibrium with the surrounded phases and suggested metasomatic infiltration from the migmatites and different dikes and veins as the source of k-feldspar in these rocks. We follow this interpretation here. The presence of zoned post-tectonic magnetite porphyroblasts in CS_3 (Table 4) may indicate that these porphyroblasts formed due to fluid infiltration (Westendorp et al., 1991). Both, k-feldspar and magnetite are not considered to be part of the parageneses considered here and will not be discussed further.

6.2. Fluid composition during the metamorphism

The discussion above was performed on hand of the grid shown in Fig. 7, assuming that all phases occur as pure end members. However, in the Solaf rocks, all calc-silicate phases occur in solid solution with some Fe and Mg. Thus, to constrain on the composition of the fluid during the metamorphism in more detail, activity corrected T-XCO_2 grids (Fig. 8) were calculated for six samples of the three different calc-silicate groups (F33 and F33a from CS_1, F89 and F51b from CS_2 and F87 and F88 from CS_3). These grids were calculated for the activities cited in the figure caption. With the temperature increasing, Fig. 8 shows that the clinozoisite absent invariant points move toward high XCO_2 values along reaction (6): q + cc = wo + CO_2. This means that the mineral assemblage of CS_1 and CS_2 buffered the composition of the fluids along reaction

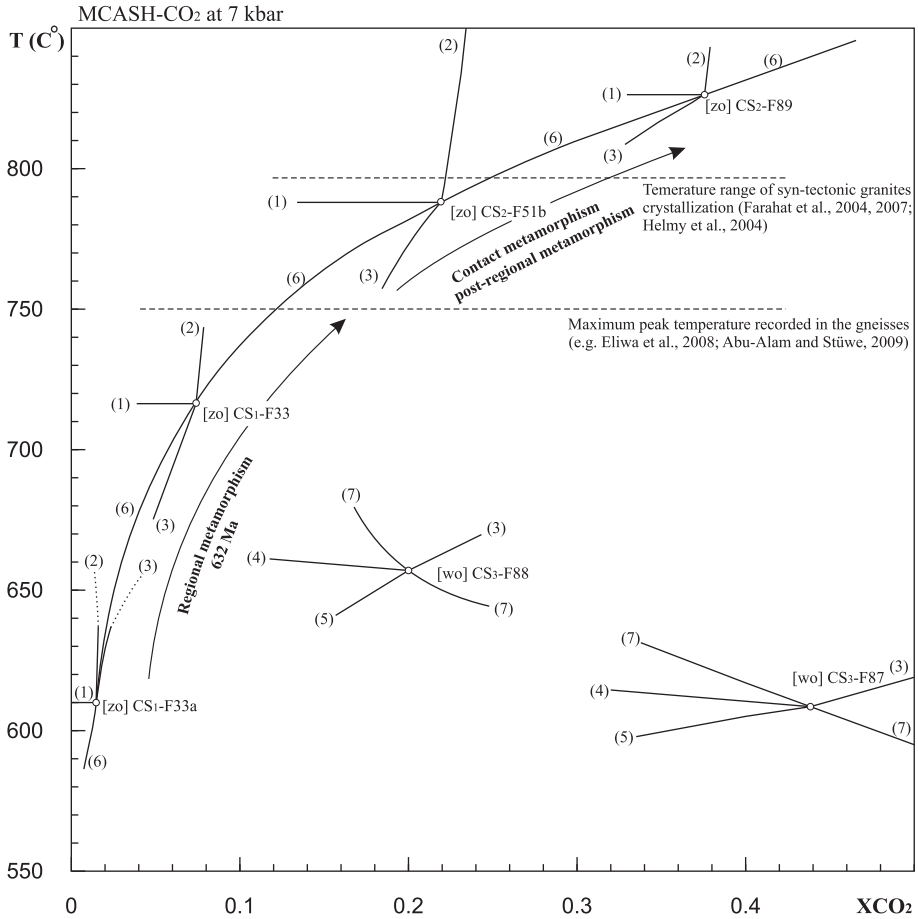

Fig. 8. Activity-corrected isobaric T-XCO_2 diagram at 7 kbar for the different calc-silicate groups. Mineral activities which were used are (an:0.031; di:0.76; gr:0.2) for F33a, (an:0.07; di:0.603; gr:0.15) for F33, (an:0.464; di:0.742; gr:0.52) for F51b, (di:0.747; gr:0.79) for F89, (an:0.55; di:0.66; gr:0.036; zo:0.4) for F87 and (an:0.7; di:0.61; gr:0.19; zo:0.61) for F88. Reaction numbers are as in Fig. 7.

(6). In addition, Fig. 8 shows that the CS_1 calc-silicates reached their peak conditions at temperature 610–720 °C and XCO_2 = 0.02–0.08. The CS_2 samples had XCO_2 equal to 0.22–0.41 at temperature 790–828 °C while CS_3 attained the peak metamorphism at temperature 600–660 and XCO_2 = 0.2–0.44.

Interestingly, the different groups record different peak conditions. CS_1 and CS_3 have the same peak temperature (610–720 °C), this temperature range is corresponding to the peak metamorphism of the surrounded gneisses (Eliwa et al., 2008; Abu-Alam and Stüwe, 2009). In addition these groups show deformation textures (e.g. deformed porphyroblasts which are embedded in deformed matrix). These textures indicate that CS_1 and CS_3 were affected by the deformation accompanied the regional metamorphism. On the other hand, the presence of large idiomorphic garnet porphyroblasts which are grown in un-deformed matrix of the CS_2 may indicates that this rock type was affected by contact metamorphism during intrusion of the syn-tectonic granites. As well as the temperature which is recorded in the CS_2 (790–828 °C) is in the crystallization range of the syn-tectonic granites (~795 °C (Farahat et al., 2004, 2007; Helmy et al., 2004)).

7. Conclusions

In conclusion, Wadi Solaf calc-silicate can be divided into three groups (CS_1, CS_2 and CS_3) according to mineral composition, mineral textures and whole rock chemistry. The rocks were affected by single (Abu-Alam and Stüwe, 2009) regional metamorphic cycle (632 ± 3 Ma) (Stern and Manton, 1987) followed by the intrusion of syn-tectonic granites at mid-crustal level (7–8 kbar). The regional metamorphism is recorded in CS_1 and CS_3 while CS_2 records the contact metamorphism. The peak conditions during the regional metamorphism cycle are 600–720 °C and XCO_2 equal to 0.02–0.08 and 0.2–0.44 for the CS_1 and CS_3, respectively. The mineral assemblage of CS_1 and CS_2 buffered the composition of the fluids along the reaction: q + cc = wo + CO_2. The rocks reached a peak contact metamorphism conditions at temperature 790–828 °C and XCO_2 = 0.22–0.41. During the contact metamorphism and the intrusion of syn-tectonic granites, the study area was intruded by several dikes and veins. This intrusion was associated by fluid infiltration process which formed post-tectonic disequilibrium phases such as k-feldspar porphyroblasts and zoned magnetite crystals. Presence of the prehnite in CS_3, suggests that Wadi Solaf calc-silicates re-equilibrated at temperature 296–311 °C during the cooling path.

Acknowledgements

This project was supported by the Austria exchange service (ÖAD) scholarship. We thank F. Makroum, A. Shalaby, M. El-Shafei and Y.M. Sultan for their help during the field work. Help with the T-XCO_2 grids by F. Gallien is appreciated. The first anonymous reviewer and B. Bonin are thanked for their constructive reviews. S. Muhongo is appreciated for his constructive suggestions and efficient editorial handling of the manuscript.

References

Abd El-Naby, H., Frisch, W., Siebel, W., 2008. Tectono-metamorphic evolution of the Wadi Hafafit Culmination (central Eastern Desert, Egypt). Implication for Neoproterozoic core complex exhumation in NE Africa. Geologica Acta 6, 293–312.

Abu-Alam, T.S., Stüwe, K., 2009. Exhumation during oblique transpression: an example from the Feiran–Solaf region, Egypt. Journal of Metamorphic Geology 27, 439–459.

Akaad, M.K., El-Gaby, S., Abas, A.A., 1967a. Geology and petrography of the migmatites around Feiran Oasis, Sinai. Bulletin Faculty of Sciences, Assiut University 10, 67–87.

Akaad, M.K., El-Gaby, S., Abas, A.A., 1967b. On the evolution of Feiran migmatites, Sinai. Journal of Geology (UAR) 11 (2), 49–58.

Beyth, M., Stern, R.J., Altherr, R., Kröner, A., 1994. The late Precambrian Timna igneous complex, Southern Israel: evidence of comagmatic-type sanukitoid monzodiorite and alkali granite magma. Lithos 31, 103–124.

Bickle, M.J., McKenzie, D., 1987. The transport of heat and matter by fluids during metamorphism. Contributions to Mineralogy and Petrology 95, 384–392.

Brady, J.B., 1988. The role of volatiles in the thermal history of metamorphic terranes. Journal of Petrology 29, 1187–1213.

Cartwright, I., Buick, I.S., 1995. Formation of wollastonite-bearing marbles during late regional metamorphic channelled fluid flow in the Upper Calcsilicate Unit of the Reynolds Range Group, central Australia. Journal of Metamorphic Geology 13, 397–417.

Deer, W.A., Howie, R.A., Zussman, J., 1992. An Introduction to the Rock Forming Minerals. Longman Scientific Technical, Harlow, United Kingdom. 696 pp..

El-Gaby, S., Ahmed, A.A., 1980. The Feiran–Solaf gneiss belt, SW of Sinai, Egypt. In: Coory, P.G., Tahoun, S.A (Eds.). Evolution and Mineralization of the Arabian–Nubian Shield. Institute of Applied Geology (Jeddah), vol. 4. pp. 95–105.

Eliwa, H.A., Abu El-Enen, M.M., Khalaf, I.M., Itaya, T., Murata, M., 2008. Metamorphic evolution of Neoproterozoic metapelites and gneisses in Sinai, Egypt: insights from petrology, mineral chemistry and K–Ar age dating. Journal of African Earth Sciences 51, 107–122.

El-Shafei, M.K., Kusky, T.M., 2003. Structural and tectonic evolution of the Neoproterozoic Feiran–Solaf metamorphic belt, Sinai Peninsula: implications for the closure of the Mozambique Ocean. Precambrian Research 123, 269–293.

Farahat, E.S., Abdel Ghani, M.S., Ahmed, A.F., 2004. Mineral chemistry as a guide to magmatic evolution of I- and A-type granitoids, Eastern Desert, Egypt. In: Proceedings of the 6th International Conference on Geochemistry. Alexandria University, Egypt, pp. 1–23.

Farahat, E.S., Mohamed, H.A., Ahmed, A.F., El-Mahallawi, M.M., 2007. Origin of I- and A-type granitoids from the Eastern Desert of Egypt: implications for crustal growth in the northern Arabian–Nubian Shield. Journal of African Earth Sciences 49, 43–58.

Fowler, A., Hassan, I., 2008. Extensional tectonic origin of gneissosity and related structures of the Feiran–Solaf metamorphic belt, Sinai, Egypt. Precambrian Research 164, 119–136.

Fritz, H., Dallmeyer, D.R., Wallbrecher, E., Loizenbauer, J., Hoinkes, G., Neumayr, P., Khudeir, A.A., 2002. Neoproterozoic tectonothermal evolution of the Central Eastern Desert, Egypt: a slow velocity tectonic process of core complex exhumation. Journal of African Earth Sciences 34, 137–155.

Fritz, H., Wallbrecher, E., Khudeir, A.A., Abu El-Ela, F., Dallmeyer, D.R., 1996. Formation of Neoproterozoic metamorphic core complexes during oblique convergence (Eastern Desert, Egypt). Journal of African Earth Sciences 23, 311–323.

Grant, J.A., 2005. Isocon analysis: a brief review of the method and applications. Physics and Chemistry of the Earth 30, 997–1004.

Greenwood, H.J., 1967. Mineral equilibria in the system MgO–SiO_2–H_2O–CO_2. In: Abelson, P.H. (Ed.), Res Geochem 2. John Wiley & Sons, New York, pp. 542–567.

Greenwood, H.J., 1975. Buffering of pore fluids by metamorphic reactions. American Journal of Science 275, 573–593.

Harley, S.L., Buick, I.S., 1992. Wollastonite–scapolite assemblages as indicator of granulite pressure–temperature–fluid histories: the Rauer Group, East Antarctica. Journal of Petrology 33, 693–728.

Harley, S.L., Fitzsimons, I.C.W., Buick, I.S., 1994. Reactions and textures in wollastonite–scapolite granulites and their significance for pressure–temperature–fluid histories of high-grade terranes. Precambrian Research 66, 309–323.

Hartmann, K., Wirth, R., Markl, G., 2008. P-T-X-controlled element transport through granulite-facies ternary feldspar from Lofoten, Norway. Contributions to Mineralogy and Petrology 156, 359–375.

Hashad, M.H., Hassen, I.S., El-Kalioubi, B., 2001. Petrology and mineralogy of calc-silicate gneisses and their significance as indicator of metamorphism in Southeastern Sinai. Egyptian Mineralogist 13, 187–223.

Helmy, H.M., Ahmed, A.F., El Mahallawi, M.M., Ali, S.M., 2004. Pressure, temperature and oxygen fugacity conditions of calc-alkaline granitoids, Eastern Desert of Egypt, and tectonic implications. Journal of African Earth Sciences 38 (3), 255–268.

Hoisch, T.D., 1985. The solid solution chemistry of vesuvianite. Contributions to Mineralogy and Petrology 89, 205–214.

Holland, T.J.B., Powell, R., 1998. An internally consistent thermodynamic dataset for phases of petrological interest. Journal of Metamorphic Geology 16, 309–343.

Loizenbauer, J., Wallbrecher, E., Fritz, H., Neumayr, P., Khudeir, A.A., Kloetzli, U., 2001. Structural geology, single zircon ages and fluid inclusion studies of the Meatiq metamorphic core complex: implications for Neoproterozoic tectonics in the Eastern Desert of Egypt. Precambrian Research 110, 357–383.

Moore, J.M., 1979. Tectonics of the Najd Transcurrent Fault System, Saudi Arabia. Journal of the Geological Society of London 136, 441–454.

Powell, R., Holland, T.J.B., 1988. An internally consistent thermodynamic dataset with uncertainties and correlations: 3. Application, methods, work examples and a computer program. Journal of Metamorphic Geology 6, 173–204.

Shaw, R.K., Arima, M., 1996. High-temperature metamorphic imprint on calc-silicate granulites of Rayagada, Eastern Ghats, India: implication for the isobarc cooling path. Contributions to Mineralogy and Petrology 126, 169–180.

Stern, R.J., 1985. The Najd fault system, Saudi Arabia and Egypt: a Late Precambrian rift-related transform system? Tectonics 4, 497–511.

Stern, R.J., Hedge, C.E., 1985. Geochronologic and isotopic constraints on late Precambrian crustal evolution in the Eastern Desert of Egypt. American Journal of Sciences 285, 97–127.

Stern, R.J., Manton, W.I., 1987. Age of Feiran basement rocks, Sinai: implications for late Precambrian crustal evolution in the northern Arabian–Nubian Shield. Journal of the Geological Society, London 144, 569–578.

Ulmer, P., 1986. NORM-Program for Cation and Oxygen Mineral Norms. Computer Library, Institute für Mineralogie und Petrographie, ETH-Zentrum, Zürich, Switzerland.

Westendorp, R.W., Watkinson, D.V., Jonasson, I.R., 1991. Silicon-bearing zoned magnetite crystals and the evolution of hydrothermal fluid at the Ansil Cu–Zn mine, Rouyn-Noranda, Quebec. Economic Geology 86, 1110–1114.